Published in final edited form as:
Ann Biomed Eng. 2010 February ; 38(2): 326–344. doi:10.1007/s10439-009-9807-x.

High-Resolution Fluid–Structure Interaction Simulations of Flow Through a Bi-Leaflet Mechanical Heart Valve in an Anatomic Aorta

Iman Borazjani[1], **Liang Ge**[2], and **Fotis Sotiropoulos**[1]

[1]St. Anthony Falls Laboratory, Department of Civil Engineering, University of Minnesota, Minneapolis, MN, USA

[2]Department of Surgery, University of California San Francisco, San Francisco, CA, USA

Abstract

We have performed high-resolution fluid–structure interaction simulations of physiologic pulsatile flow through a bi-leaflet mechanical heart valve (BMHV) in an anatomically realistic aorta. The results are compared with numerical simulations of the flow through an identical BMHV implanted in a straight aorta. The comparisons show that although some of the salient features of the flow remain the same, the aorta geometry can have a major effect on both the flow patterns and the motion of the valve leaflets. For the studied configuration, for instance, the BMHV leaflets in the anatomic aorta open much faster and undergo a greater rebound during closing than the same valve in the straight axisymmetric aorta. Even though the characteristic triple-jet structure does emerge downstream of the leaflets for both cases, for the anatomic case the leaflet jets spread laterally and diffuse much faster than in the straight aorta due to the aortic curvature and complex shape of the anatomic sinus. Consequently the leaflet shear layers in the anatomic case remain laminar and organized for a larger portion of the accelerating phase as compared to the shear layers in the straight aorta, which begin to undergo laminar instabilities well before peak systole is reached. For both cases, however, the flow undergoes a very similar explosive transition to the small-scale, turbulent-like state just prior to reaching peak systole. The local maximum shear stress is used as a metric to characterize the mechanical environment experienced by blood cells. Pockets of high local maximum shear are found to be significantly more widespread in the anatomic aorta than in the straight aorta throughout the cardiac cycle. Pockets of high local maximum shear were located near the leaflets and in the aortic arc region. This work clearly demonstrates the importance of the aortic geometry on the flow phenomena in a BMHV and demonstrates the potential of our computational method to carry out image-based patient-specific simulations for clinically relevant studies of heart valve hemodynamics.

Keywords

Heart valve; Mechanical heart valve; Bi-leaflet mechanical heart valve; Pulsatile flow; Simulation; Fluid–structure interaction; Anatomic aorta; Immersed boundary

Address correspondence to Fotis Sotiropoulos, St. Anthony Falls Laboratory, Department of Civil Engineering, University of Minnesota, Minneapolis, MN, USA. fotis@umn.edu.

INTRODUCTION

Heart valve replacement is a common surgical practice to improve the condition of patients with heart valve disease. Annually there are more than 100,000 valve replacements in the US alone[19] and among the replaced valves more than half are using mechanical heart valves (MHV). Mechanical valves are typically made from pyrolytic-carbon and, due to the man-made nature of the valve material, have outstanding durability. All current MHVs, however, are strongly thrombogenic. Recipients of MHVs rely on anti-coagulation treatment to reduce the thromboembolism threat and poorly managed anti-coagulation treatment often leads to life-threatening hemorrhage. Such limitations seriously reduce the life-quality of MHV recipients and ongoing research activities are focusing on reducing the risk of thromboembolism through valve design improvement.

Although the exact mechanism leading to thromboembolism in MHVs is not fully understood, it has been well documented that hemodynamic factors, such as shear stress, flow separation and turbulence, can directly or indirectly lead to thrombus formation and eventually thromboembolism events. The strong links between hemodynamics and thromboembolism have led to a very large number of *in vitro* and *in vivo* experimental studies of the MHV-induced hemodynamics. For example, Chandran *et al.*[4] measured the velocity and turbulent shear stress profiles in regions near prosthetic valves under physiological pulsatile conditions. Yoganathan *et al.*[40] measured the Reynolds stress distribution in the vicinity of 13 different prosthetic heart valves. Ellis *et al.*[9] conducted experiments to study the micro-flow field within the hinge region of a Medtronic Parallel bileaflet valve. Liu *et al.*[26] documented the turbulence characteristics, including turbulent length scales, turbulent stresses and turbulent kinetic energy spectrum, etc., under pulsatile flow conditions using particle image velocimetry (PIV). Manning *et al.*[27] used PIV to measure the *in vitro* regurgitant flow through a St. Jude Medical (SJM) bileaflet valve under physiological flow conditions. Nygaard *et al.*[31] carried out *in vivo* measurements of the turbulent stresses downstream of three different MHVs (an SJM valve, a CarboMedics valve and a Starr-Edwards rubber ball valve) implanted in humans using a pulsed Doppler ultrasound system. Nyboe *et al.*[30] have used the same method to measure the *in vivo* distribution of turbulent stresses under different cardiac output conditions in pigs. In addition to the aforementioned experimental measurements, a host of computational fluid dynamics (CFD) simulations have also been conducted to study the valve-induced hemodynamics. Huang *et al.*[20] simulated the blood flow through a tilt-disc valve using 2D CFD simulations. King *et al.*[23] conducted 3D simulations of the flow through a bileaflet valve. Ge *et al.*[12] studied the 3D flow induced by a bileaflet MHV under steady incoming conditions. Grigioni *et al.*[17] simulated 3D flow through a bileaflet valve during the first half of the systolic phase. Fluid/structure interaction simulations were carried out in 2D[5] and 3D[6] studies.

In spite of the large and rapidly expanding body of literature dedicated to the study of heart valve hemodynamics, our understanding of the actual mechanical environment that is responsible for valve-induced blood cell damage is still limited (see also related discussion in Ge *et al.*[11]). The main reason for this is that the majority of previous studies focused on quantifying the distribution of the Reynolds stresses in MHV flows due to the prevailing wisdom in the literature that turbulent stresses are the main culprit for inducing blood cell damage. Such an assumption, however, is questionable because the mechanically induced blood cell damage can only be caused by mechanical force and Reynolds stress is not related to any physical force. It is rather a statistical quantity developed to quantitatively describe turbulent flows and as such it can not possibly induce physical damage to blood cells. We extensively discussed these issues in Ge *et al.*[11] and further pointed out that the only physical force experienced by suspended blood cells is caused by viscous effects, which are

quantitatively represented only by the viscous shear stresses. It should be noted that extra physical force could arise if the Kolmogorov scale (i.e., the size of the smallest vortices in a turbulent flow) of the flow through a BMHV is comparable with the size of suspended blood cells. As we noted in Ge *et al.*,[11] however, the Kolmogorov scale in a BMHV flow field is much larger than the size of blood cells. The study in Ge *et al.*[11] clearly indicates the need for a research paradigm shift from the traditional approach focusing on turbulence statistics to an approach that can accurately quantify the instantaneous hemodynamic environment in terms of the viscous shear stress. This, however, can only be accomplished by obtaining at high-resolution the spatial distribution of the 3D instantaneous velocity field.

Following this new research paradigm, a number of experimental and computational studies have recently been reported focusing on the instantaneous flow environment in MHVs. The instantaneous flow field downstream of the leaflets of an SJM Regent 23mm bileaflet valve was recently investigated using high-resolution PIV in tandem with high-resolution numerical simulations with prescribed leaflet kinematics. [7] The PIV measurements were carried out on the plane of symmetry that cuts across the two leaflets and yielded the first detailed insights into the instantaneous vorticity dynamics of the flow—including the complicated, albeit laminar and organized, flow patterns during early systole, the subsequent instability of the leaflet shear layers at approximately the middle of the accelerating phase, and the sudden eruption of the flow into a small-scale, turbulent-like state just as peak systole is approached. The numerical simulations reproduced all these experimental findings with good accuracy and further elucidated for the first time the three-dimensional structure of the flow.[7] The numerical method used to carry out the numerical simulations in Dasi *et al.*[7] is the curvilinear, immersed-boundary (CURVIB) method developed by Ge and Sotiropoulos.[13] The experimental and computational data sets obtained in Dasi *et al.*[7] were subsequently analyzed in detail to quantify the instantaneous shear stress environment and address its potential hemodynamic implications in Ge *et al.*[11] Recently the CURVIB method was extended further to develop a powerful fluid/structure interaction (FSI) formulation (the CURVIB-FSI method) for carrying out fully coupled direct numerical simulations of MHV flows.[2] The computed results reported in Borazjani *et al.*[2] were in excellent agreement with the experiments,[7] both in terms of the instantaneous flow patterns and the calculated leaflet kinematics. It is important to point out, however, that in all these studies the aorta geometry was oversimplified and assumed to be a straight circular pipe while the triple-sinus geometry was modeled with a simple circular cavity placed right downstream of the valve (a more detailed sketch of the *in vitro* geometry can be found in Dasi *et al.*[7]). Given the complexity and high degree of three-dimensionality of a realistic anatomic aorta, it is unlikely that such an over-simplified sinus/aorta geometry will yield results that are relevant to *in vivo* flow conditions.

The objective of this paper is to carry out the first high-resolution fluid–structure interaction direct numerical simulation of BMHV-induced hemodynamics in an anatomically realistic aorta. The aorta/valve model was constructed by reconstructing an anatomically realistic aorta geometry using magnetic resonance imaging (MRI) and subsequently inserting an SJM Regent bileaflet valve into the aortic valve position. A numerical simulation was subsequently carried out to study the motion of valve leaflets and the fluid dynamics induced by the valve. A physiological flow waveform was prescribed at the inlet of the aorta upstream of the valve and the motion of the two leaflets is simulated using the CURVIB-FSI method developed in Borazjani *et al.*[2] The aorta wall, however, was modeled as a rigid wall and the FSI between the aorta and blood flow was not considered. Note that in recent years, hemodynamic studies using image-based CFD simulations, such as the one reported herein, have been successfully applied to study blood flow in an aneurysm[36] and an anatomic total cavopulmonary connection (TCPC),[32] among many others.[28,38] To the best of our knowledge, however, this work is the first attempt to investigate the MHV-induced

hemodynamics in a patient-specific aorta anatomy. Such a step is important because the valve-induced hemodynamics is strongly affected by the valve, the downstream sinus, and the aorta geometries.[10,15,24,40] Therefore, such an image-guided CFD simulation is also a very important step toward the goal of patient-specific MHV implantation planning, during which different implantation orientations and different valves could be compared and the best valve type with the best implantation orientation could be identified before surgery.

This paper is organized as follows. In the “Governing Equations and the Numerical Method” section, we briefly describe the numerical method and give the computational details about the geometry, grid, time step, etc., in the “Computational Details” section. In the “Results” section, we report the results of the simulations in terms of the leaflet kinematics and flow physics in the anatomic aorta and compare it with the straight aorta results. Finally, in the “Discussion” section, we discuss the key findings of this work.

GOVERNING EQUATIONS AND THE NUMERICAL METHOD

The governing equations for the fluid (blood) domain are the three-dimensional, unsteady incompressible continuity and Navier–Stokes equations, which in compact tensor notation read as follows:

$$\frac{\partial u_i}{\partial x_i}=0$$
$$\frac{Du_i}{Dt}=-\frac{\partial p}{\partial x_i}+\frac{1}{Re}\frac{\partial^2 u_i}{\partial x_j \partial x_j} \quad (1)$$

where u_i are the Cartesian velocity components, p is the pressure divided by the density ρ, and Re is the Reynolds number of the flow based on a characteristic length and velocity scale. D/Dt is the material derivative defined as:

$$\frac{D}{Dt}(\cdot)=\frac{\partial}{\partial t}(\cdot)+u_j\frac{\partial}{\partial x_j}(\cdot) \quad (2)$$

In Eq. (1) blood has been assumed to be Newtonian, which is a valid assumption for flows in large arteries such as the aorta. For a BMHV implanted in the aortic position, however, there are small regions of the flow domain (valve hinges and leakage jet during closure) within which non-Newtonian effects could become important and should be taken into account in the governing equations. Modeling of these fine, albeit potentially important from a hemodynamic standpoint, flow features is beyond the scope of this work. Furthermore, the aortic lumen is assumed to be rigid and the motion of the left ventricle upstream of the aortic valve has been simplified by prescribing a physiological waveform inflow at the inlet of an attached pipe—see “Computational Details” section below.

The motion of the leaflets is governed by the angular momentum equation around the hinge axis, which after non-dimensionalization reads as follows:

$$\frac{\partial^2\theta}{\partial t^2}+\zeta\frac{\partial\theta}{\partial t}=\frac{1}{I_{\text{red}}}C_3 \quad (3)$$

In the above equation, $\theta = \theta(t)$ is the leaflet angle defined as in Fig. 1, which can vary between $\theta_{\min} = 4.75°$ and $\theta_{\max} = 58.75°$. I_{red} is the leaflet reduced moment of inertia defined as:

$$I_{\text{red}}=\frac{\rho_s I_{xx}}{\rho_f D^5} \tag{4}$$

where D is diameter of the aorta, ρ_f is the density of the fluid, ρ_s is the density of the leaflet material, and $I_{xx} = \int r^2 dV$ (with $r=\sqrt{(y-y_h)^2+(z-z_h)^2}$; y_h and z_h position of the hinge axis; and dV as the infinitesimal volume element) is the product of inertia around the leaflet's hinge axis. The damping coefficient is defined as

$$\zeta=\frac{cD}{I_{xx}U} \tag{5}$$

where c is the damping factor and U is the maximum bulk flow velocity at inlet. The moment coefficient exerted by the flow on the leaflet is defined as

$$C_{\Im}=\frac{\Im_1}{\rho_f U^2 D^3} \tag{6}$$

where $\Im_1$ is the moment around the hinge axis, which is aligned with the $i = 1$, i.e., x direction. Note that as in the straight aorta case,[2,7] we have assumed that the hinge axis is in the direction of gravity. Therefore, gravity has no effect on the moment around the hinge axis. $\Im_i$ is calculated by integrating the moment of pressure and viscous forces as follows:

$$\Im_i(t)=\int -\varepsilon_{ijk} r_j p n_k dA+\int \varepsilon_{ijk} r_j \tau_k n_l dA \tag{7}$$

where p is pressure, τ_{ij} is the viscous stress tensor, n_i is the ith component of normal vector to the immersed surface element dA, and r_i is ith component of position vector of the immersed surface element from the rotation axis. ε_{ijk} is called the alternating unit tensor defined as:

$$\varepsilon_{ijk}=\begin{cases} 1 & \text{if } ijk=123, 231, \text{or } 312 \\ 0 & \text{if any two indices are alike} \\ -1 & \text{if } ijk=321, 213, \text{or } 132 \end{cases} \tag{8}$$

Equation (3) comprise a system of second-order ordinary differential equations. Numerically these equations are typically solved by first transforming them into a system of first-order ordinary differential equations as follows:

$$\frac{\partial\theta}{\partial t}=\omega \tag{9}$$

$$\frac{\partial\omega}{\partial t}=\frac{C_{\Im}}{I_{\text{red}}}-\zeta\omega \tag{10}$$

The fluid and structure dynamics are coupled together at the fluid/structure interface Γ by the following boundary conditions:

$$\vec{u}=\vec{U}=\vec{n}\frac{\partial\theta}{\partial t}\times\vec{r} \quad \text{at} \quad \Gamma \tag{11}$$

where $\vec{u}$ and $\vec{U}$ is the velocity of fluid and solid at the interface, respectively. $\vec{r}$ is the position vector from the hinge and $\vec{n}$ is the hinge axis vector around which the leaflets rotate. Equation (11) couples the Eulerian velocity field of the fluid with the Lagrangian description of the motion of the solid surface and closes the fluid–structure interaction problem, comprising of Eqs. (1), (3), and (11), which needs to be solved numerically.

The FSI solver adopts the partitioned FSI solution approach and both loose (LC-FSI) and strong (SC-FSI) coupling strategies are implemented (see Borazjani *et al.*[2] for details). Numerical experiments and theoretical stability considerations presented in Borazjani *et al.*[2] suggest that both the properties of the structure (mass, geometry) and the local flow conditions can play an important role in determining the stability of the FSI algorithm. Under certain conditions, e.g., opening phase of the leaflets, unconditionally unstable FSI iterations result even when SC-FSI is employed. For such cases, however, combining SC-FSI with under-relaxation in conjunction with the Aitken acceleration technique[22] was shown to effectively resolve the stability problems. The under-relaxation equation reads as follows[2]:

$$\tilde{\omega}^{\ell+1}=(1-\alpha)\tilde{\omega}^{\ell}+\alpha\omega^{\ell+1} \tag{12}$$

where α is the under-relaxation coefficient ($0 \le \alpha \le 1$), whose value is known to largely determine the overall convergence rate of SC-FSI iterations. The value of α is determined by the Aitken acceleration technique as follows[2,29]:

$$\Delta\tilde{\omega}^{\ell+1}=\tilde{\omega}^{\ell}-\omega^{\ell+1} \tag{13}$$

$$\lambda^{\ell+1}=\lambda^{\ell}+(\lambda^{\ell}-1)\frac{\delta\tilde{\omega}^{\ell+1}}{\Delta\tilde{\omega}^{\ell}-\Delta\tilde{\omega}^{\ell+1}} \tag{14}$$

$$\alpha=1-\lambda^{\ell+1} \tag{15}$$

For the first iteration ($\ell = 1$), $\Delta\tilde{\omega}^{\ell+1}$ can be calculated while the $\lambda^{\ell+1}$ cannot be calculated and a preset value of $\lambda = 0.3$ is used to calculate the first under-relaxation coefficient α.

The SC-FSI is declared to be converged when the difference in the angular velocity and position of each leaflet between two successive iterations drops about 4 orders of magnitude to 10^{-6}. Such a level of convergence is usually achieved within 4–5 SC-FSI iterations with the Aitken acceleration technique. For more details on our FSI numerical method, the reader is referred to Borazjani *et al.*[2]

The Navier–Stokes and continuity equations, Eq. (1), in a domain containing multiple, 3D, arbitrarily complex moving immersed boundaries are solved using the sharp-interface CURVIB solver of Ge and Sotiropoulos. [13] In the CURVIB approach a curvilinear grid

system is adopted to serve as the background grid and the immersed bodies are treated as sharp-interface immersed boundaries. The sharp-interface immersed boundary method, enhanced with an efficient node classification algorithm described in Borazjani *et al.*,[2] can easily handle large movements/deformations of multiple immersed bodies and is shown to be second-order accurate.[3,14] The curvilinear background mesh is adopted to enhance algorithmic flexibility and efficiency for internal flow problems in which the background domain can be efficiently discretized with a boundary-conforming curvilinear mesh (see Ge and Sotiropoulos[13] for details).

Our CURVIB solver employs a novel, fully-curvilinear staggered grid discretization approach, which does not require either the explicit evaluation of the Christoffel operators or the discretization of all three momentum equations at cell interfaces as done in previous curvilinear staggered grid formulations. The equations are integrated in time using an efficient, second- order accurate fractional step methodology coupled with a Jacobian-free, Newton–Krylov solver for the momentum equations and a GMRES solver enhanced with multigrid as preconditioner for the Poisson equation. Formore details about the fluid solver the readers are referred to Ge and Sotiropoulos.[13]

COMPUTATIONAL DETAILS

The anatomic aorta geometry was provided to us by the Cardiovascular Fluid Mechanics Laboratory at the Georgia Institute of Technology and was reconstructed from an MRI of a healthy volunteer with a method similar to de Zélicourt *et al.*[8] The main aortic branches on the aortic arch, i.e., the coronary arteries, the innominate artery, the left and right carotids, and the left subclavian artery, were removed to simplify the outflow condition. Similar to the straight aorta model,[2] the inlet is a straight circular pipe $4 \times D$ long while the outlet is also a straight pipe $2.25 \times D$ long extended after the aortic arc with a cross-section identical to the cross-section at the end of the anatomic aorta MRI data (see Fig. 2).[1] The circular inlet was chosen to achieve a symmetric inflow similar to our previous straight aorta simulations. A body-fitted curvilinear grid with $201 \times 201 \times 253 \approx 10^7$ grid nodes was used to discretize the empty aorta as shown in Fig. 3. All of the anatomic aorta simulation parameters and assumptions were identical to the straight aorta simulations reported in Borazjani *et al.*[2] to facilitate the comparison between the anatomic and straight aorta results. As in straight aorta simulations of Borazjani *et al.*,[2] we neglected the hinge mechanism connecting the leaflets and the valve housing. In addition, the damping due to the friction of the hinge was neglected as well since it is very small relative to the flow forces and no experimental data are currently available on the actual value of the friction coefficient. At the outflow we used the convective boundary condition similar to the straight aorta geometry.[2] At the inflow we prescribed unsteady, pulsatile plug flow based on the experimental data reported in Dasi *et al.*[7] Figure 4 shows the corresponding experimental time history of the flow rate within a cardiac cycle with the peak flow rate of 24.27 L/min. We simulated one cardiac cycle, which according to the experiment[7] has the time period of 860 ms and the peak Reynolds number of 6000 based on the upstream pipe diameter (25.4 mm) and peak bulk velocity. The physical time step of $\Delta t = 0.33$ ms, corresponding to about 2580 time steps per cardiac cycle, used in the anatomic simulations is identical to the straight aorta simulations.[1,2]

The valve and the housing geometry (clinical quality St. Jude Regent 23 mm valve) were discretized with a triangular mesh, as required by the CURVIB method, which is identical to that used in the straight aorta case.[2] The reduced-inertia of the valve in both the anatomic and straight aorta cases is the same, i.e., $I_{red} = 0.001$, which was calculated by assuming Polycarbonate as the leaflet material with a density of 1750 kg/m^3 and blood density of 1030 kg/m^3. The valve leaflets and the housing were placed into the body-fitted mesh, used to discretize the anatomic aorta, as immersed bodies between the end of the straight inlet

section and the sinus area of the anatomic arch section as shown in Fig. 3. Due to the low reduced-inertia of the leaflets, loose- and strong-coupling are expected to be unstable as illustrated in Borazjani *et al.*[2] Therefore, the simulations were performed using under-relaxation, Eq. (12), with the Aitken convergence acceleration technique Eqs. (13)–(15).[2]

RESULTS

In this section we present the results of FSI simulations of a BMHV implanted in an anatomically realistic aorta and compare the results with our previous FSI simulations of the same valve implanted in a simplified straight and axisymmetric aorta.[2] As mentioned above, for both cases we used exactly the same valve (23 mm St. Jude Medical Regent bileaflet valve) and identical inlet flow conditions. Therefore, the computed flowfields can be readily juxtaposed to highlight the similarities and differences between the two cases and investigate the importance of the aorta geometry on heart valve hemodynamics.

Convergence of FSI Iterations

As we have extensively discussed in Borazjani *et al.*,[2] obtaining converged FSI iterations for the BMHV problem is a particularly challenging task because of the combined effects of the leaflet properties (very low reduced inertia) and local flow effects. The low reduced inertia of the leaflets causes the motion of the leaflets to be dominated by the added-mass effect, which in general has a detrimental effect on the stability of FSI iterations. We found that the under-relaxed SC-FSI combined with the Aitken acceleration technique Eqs. (12)–(15) could yield converged FSI iteration.[2] We find these conclusions to also be valid for the current study. To gauge the ability of our method to yield robust and fully-converged FSI iterations for the anatomic case, we show in Fig. 5 the convergence rate of the SC-FSI with the Aitken acceleration technique for several physical time steps during the opening phase of the cardiac cycle (which as discussed in Borazjani *et al.*[2] is the most challenging from the numerical stability standpoint). The residual in this figure was defined as the difference between the angular velocity of two successive SC-FSI iterations. The figure shows that, similar as the straight aorta simulations,[2] 4–5 SC-FSI iterations were enough to reduce the residual by 4–5 orders of magnitude in the current anatomic aorta simulations (see Fig. 5).

Calculated Leaflet Kinematics

The calculated leaflet kinematics for the anatomic case as well as the pressure drop through the valve for both anatomic and straight cases is shown in Fig. 6. The pressure drop was calculated between two central points, one located before the valve and the other downstream the leaflets in the fully open position. As observed from the figure, the pressure drop increases and decreases with the incoming flow-rate and undergoes large oscillations when the leaflets become fully closed. These results are in good agreement with the experimental measurements in a straight aorta.[7] It is interesting to note that large pressure oscillations were also observed in previous experiments (see Fig. 4 of Dasi *et al.*[7]).

The two leaflets, after an initial rapid acceleration phase that lasts about 5–10 ms, were seen to transition into a constant speed state (Fig. 6), during which the angle of both leaflets grows linearly with time. Upon approaching the fully open position, the angular velocity of the leaflets slightly decreases (the St. Jude Regent valves have a fully open angle of about 5°). A striking finding of Fig. 6 is the slight albeit clearly visible rebound of Leaflet 2 (see Fig. 3 for definition of Leaflet 1 and 2) shortly after it reaches its fully open position. Leaflet 1 also undergoes a re-bound but it is too weak to be observed in the scale of Fig. 6. The two leaflets are seen to stay at the fully open position even past the time instant when the incoming flow direction reverses (approximately 350 ms from the start of the cycle) (Fig. 4). In fact valve closing does not begin until about 30 ms later at t = 380 ms. Shortly after the

fully closure of the valve, Leaflet 1 undergoes a very pronounced rebound phase, which lasts for approximately 55 ms. Note that unlike the rebound of Leaflet 2 at opening, the rebound upon valve closure is very pronounced as Leaflet 1 opens by about 10° before closing again.

The simulated kinematics of the anatomic case is somehow similar to our previously reported straight aorta case,[2] but with some subtle yet very important differences. The valve was found to open faster (by about 20 ms) but close slower (by about 4 ms) in the anatomic aorta case than in the straight aorta case (Fig. 7). In both the anatomic and straight aorta cases, the two leaflets open/close in an asymmetric fashion. The asymmetry in the anatomic case is stronger upon opening but weaker during closing phase than that of the straight aorta case. The asymmetric leaflet rebound during both opening and closing is far more pronounced in the anatomic aorta. The importance of these differences will be discussed in the “Discussion” section.

Previous experiments of a BMHV implanted in a straight aorta have demonstrated that the leaflet motion never reaches a cycle-to-cycle periodic state with the variations being most pronounced during the closing phase.[7] The valve leaflets neither open nor close symmetrically, the asymmetry being more pronounced during the closing phase.[7] In the current study we did not address the cycle-to-cycle variability of the leaflet kinematics as we have simulated only one cycle. Simulations aimed at further exploring the issue of cycle-to-cycle variability are currently under way and results will be reported through future communications. Nevertheless, the simulations have properly reproduced the asymmetric motion of the two leaflets both in the current study and in our previous investigations on the straight aorta case.[2]

2D Flow Features

The different leaflet kinematics between the straight and anatomic cases are to be expected given the major differences in aortic shape, which naturally induces to very different flow fields. To gauge the similarities and differences between the two flowfields, we compare in Fig. 8 the out-of-plane vorticity contours of the anatomic and straight aorta cases at a plane that is perpendicular to and cuts through the middle of the leaflets at various instants within a cardiac cycle. It can be observed that a characteristic triple-jet structure (two side-jets between the leaflets and the valve-housing and a central jet between the two leaflets) forms in both cases. The shear layer corresponding to the side jets rolls up into a ring like structure, which expands toward the sinus wall. By closer examination of the vorticity field along the sinus wall, it was observed that the vortex ring (V1 in Fig. 8b) extracts a secondary layer of vorticity of opposite sign near the sinus wall. The point that the vorticity changes sign along the sinus wall is the reattachment point of the side jet. The reattachment is located further downstream along the sinus wall for the straight aorta. This can be attributed to the lower jet velocities or the smaller expansion of the aorta in the anatomic case. This issue will be discussed further below. The vortex ring in both aortas travels downstream during the acceleration phase (Figs. 8a–8d) until it reattaches at the end of the sinus expansion (Fig. 8e). After this instant, as the side jets become stronger, the side jet shear layer becomes unstable yielding a complicated recirculating flow in the sinus region.

Apart from the shear layers emanating from the valve housing, each leaflet creates two shear layers as well. One shear layer forms due to the separation of the flow from the inner side (S1 in Fig. 8a) and the other due to separation from the outer side (S2 in Fig. 8a) of each leaflet—note that at the fully open position, each leaflet makes a 5 degree angle of attack with the streamwise flow. As can be seen in Fig. 8b the outer shear layer for the straight aorta rolls up along with the earlier-discussed sinus vortex ring. In the anatomic case this roll-up does not occur as the shear layers are diffused laterally toward the sinus walls. The inner shear layer follows the outer layer in the straight aorta but in the anatomic aorta two

tails from the inner layer are extended toward the outer layers. Nevertheless, leaflet shear layers in both cases travel downstream faster than those emanating from the valve housing. As the flow-acceleration continues, the leaflet shear layers become unstable and start shedding von Karman-like vortical structures (Figs. 8d and 8e) and just before the peak systole the flow breaks down into small chaotic structures (Fig. 8f), which dominate the flow even after the peak diastole (Fig. 8h). A striking finding that follows from these figures is that the leaflets shear layers in the anatomic aorta become unstable later than in the straight aorta. This trend should be partly attributed to the lower jet velocities in the anatomic aorta as explained below.

As shown in Fig. 9, which shows the cross-sectional and mid-plane views of the instantaneous velocity fields for both cases, the jet velocities at regions immediately downstream of the leaflets are practically the same in both cases (Fig. 9a). Difference, however, starts to emerge at a distance 0.5*D* downstream of the leaflets (Fig. 9b). The jets in the anatomic case appear to diffuse much faster than in the straight aorta case. This is due to two important geometric differences between the two aortas. First, the sudden area expansion in the sinus region of the anatomic aorta is significantly smaller than that of the straight aorta. The smaller sinus expansion leads to the faster jet reattachment as seen in Fig. 9c thus increasing the lateral diffusion of the side-jets and decreasing the jet flow velocity (Fig. 9c). Second, the anatomic aorta curvature induces a strong secondary motion that tends to hinder the penetration of the leaflet jets downstream (Fig. 9d). In the straight aorta, however, such a secondary motion does not exist. Consequently, the jets can easily penetrate toward the end of the sinus.

3D Vortical Structures

The three-dimensional vortical structures are visualized in Fig. 10 using the q-criterion[21] for both the straight and anatomic aortas at different time instants within the cardiac cycle. Similar to the straight aorta, the structures in the anatomic aorta are well organized and laminar in the early systole but break down in an explosive manner into small-scale chaotic vortical structures just before the peak systole. The chaotic, turbulent-like state persists throughout the rest of cardiac cycle. For the reasons explained above, it can be observed that the three-dimensional structures develop faster in the straight aorta than in the anatomic aorta (see Figs. 10a–10e). However, there is not much difference between the two cases after the flow transitions into the turbulent state (Figs. 10f, 10g, and 10h). One important feature of the anatomic case, which was not visible from the 2D vorticity contours in the mid plane, is the growth of structures in the aortic arc even in early systole (Figs. 10a and 10b). These vortical structures are created by the curvature-induced secondary currents in the arch, which is completely missing in the straight aorta case. The sinus vortex-ring formation in the anatomic aorta is also different from that of the straight aorta. In the straight aorta with a symmetric sinus the sinus vortex-ring is seen to fold forward as its central portions move downstream faster than the two sides near the hinges (Fig. 10c). For the anatomic aorta, however, the sinus ring develops a mode three azimuthal modulation, due to the triple sinus structure, and moves upward in the sinus until the shear layers of the side jets reattach to the end of the sinus expansion and small scale structures emerge in the sinus region (Fig. 10d).

Viscous Shear Stress

Naturally, the difference in the flow patterns should translate into differences in the forces experienced by blood cells in the straight and anatomic aortas. To evaluate the two flowfields in terms of the forces acting on blood cells, the instantaneous viscous stresses can be used to provide a measure of mechanical loads.[11] Since viscous stresses comprise a second-order tensor, a coordinate-independent metric is needed to quantify mechanical

loads. Similar to Grigioni *et al.*,[16] Travis *et al.*,[37] and Ge *et al.*,[11] the concept of local maximum stress is used herein as follows.

The principal stresses of a given stress tensor τ_{ij} are the solutions of the following equation:

$$\sigma^3 - I_1\sigma^2 + I_2\sigma - I_3 = 0 \tag{16}$$

where I_1, I_2, and I_3 are the first, second, and third invariants of the tensor (repeated indices imply summation):

$$I_1 = \tau_{jj} \tag{17}$$

$$I_2 = \tau_{ij}\tau_{ij} \tag{18}$$

$$I_3 = \tau_{ij}\tau_{jk}\tau_{ki} \tag{19}$$

The coordinate invariant local maximum stress τ_{loc} is given by

$$\tau_{\mathrm{loc}} = \frac{1}{2}(\sigma_{\max} - \sigma_{\min}) \tag{20}$$

where $\sigma_{\max}$ and $\sigma_{\min}$ are the maximum and minimum principal stresses.

Here we use the histogram of the local maximum shear stress values at a given instant in time to illustrate the distribution of τ_{loc} throughout the domain at that instant. In Fig. 11 we plot the histogram of τ_{loc} in an anatomic aorta at different time instants within a cardiac cycle. The histograms plot the number of occurrence of τ_{loc} values in intervals within the width of $\Delta\tau_{\mathrm{loc}}$ = 0.064 Pa, normalized by the total number of occurrences and multiplied by 100 to be stated as percentile; they can therefore be viewed as the percentile of the domain volume that has a given value of τ_{loc}. It can be observed from Fig. 11 that the histogram decays exponentially with τ_{loc} during the cardiac cycle, i.e., most of the domain experiences low τ_{loc} and the high values occur less frequently in the domain. To compare the straight and anatomic aortas in Fig. 12, we plot the histogram of τ_{loc} in the straight and anatomic aorta at different time instants during the cardiac cycle and we zoom into the high shear values between 6 and 12 (Pa). Comparing the anatomic and straight aorta during each instant shows that the anatomic aorta has higher τ_{loc} regions relative to the straight aorta. Furthermore, it can be observed that the overall histogram values correlate with the flow rate, i.e., higher flow rate corresponds to larger areas of higher τ_{loc}, since the histogram values increase from instant (a) to (f) of Fig. 12 when the flow rate increases.

To better illustrate the above points, we plot in Fig. 13 the iso-surfaces of the local maximum shear stress τ_{loc} = 6.4 Pa for several time instants during the cardiac cycle. First, in agreement with the histogram results we observe larger regions of higher τ_{loc} in the anatomic aorta at all time instants. The aorta curvature and the curvature-induced secondary motion should be the main culprits for the fact that the pockets of τ_{loc} are more frequent in the arc region of anatomic aorta than in the straight aorta. Second, again in agreement with our histogram results, the levels of τ_{loc} correlate very well with the flow rate. In both

anatomic and straight aorta as the flow rate increases toward the peak systole (see Figs. 13a–13f) larger regions of high τ_{loc} are observed. After peak systole, when the flow rate decreases, the regions of higher τ_{loc} decrease in size as well (see Figs. 13f–13h).

To further explore where regions of high τ_{loc} are, we plot in Fig. 14 the contours of τ_{loc} on the mid-plane of the valve. It is readily seen that the level of viscous shear stress closely follows the incoming flow rate and reaches maximumnear the peak systole (Fig. 14f). It can also be observed that, both in the anatomic and straight aortas, regions near the leaflets consistently exhibit high values of τ_{loc}. The rest of the domain, however, experiences low values of τ_{loc}. In the early stages of the systole, areas of high shear are larger in the straight aorta than in the anatomic aorta (Figs. 14a–14e). This is due to the fact that flow develops and breaks down much faster in the straight aorta case.

DISCUSSION

To the best of our knowledge, this work is the first-ever high-resolution FSI study of BMHV conducted in an anatomic geometry under physiologic condition— see our recent review of state-of-the-art numerical simulations of BMHV flow.[35] The current work, along with our previous work for the straight aorta,[2] contributes many new insights into the BMHV induced hemodynamics.

A critical issue in simulating BMHV FSI problems is the numerical instability arising from the coupling between the fluid and structure domains. As demonstrated in Borazjani *et al.*,[2] the current method of choice in FSI simulations is to use a partitioned approach, where the FSI problem is divided into a fluid domain problem and a structure domain problem and the two separated domains are coupled at the interfaces between them. For cases like the BMHV flow the coupling between the structure and fluid domains is inherently unstable, primarily due to large added-mass effect and low inertia of the leaflets. As shown in Borazjani *et al.*,[2] an under-relaxation scheme as Eq. (12) is critical for obtaining converged FSI iterations between the two domains. We also demonstrated in Borazjani *et al.*[2] a convergence acceleration method, such as the Aitken acceleration technique, could be applied to rapidly improve the convergence rate of the coupling. The successful application of the coupling approach with the under-relaxation method and the Aitken acceleration in the current study of BMHV in an anatomically realistic geometry clearly demonstrates the enormous potential of our numerical approach for carrying out highly-resolved simulations in patient-specific anatomies.

The overall leaflet kinematics observed in the current study agrees well qualitatively with available experimental measurements.[7,34] The opening phase is seen to undergo a three-stage motion: an initial rapid acceleration phase, a constant rotating phase and a slowly deceleration phase upon approaching the fully open position. The closing of the valve is seen to occur after the flow direction reverses. Leaflet rebound is observed both after the valve reaches the fully open position during the opening phase and fully closed position during the closing phase. In the latter case, however, the rebound is very strong for the anatomic case in which one of the two leaflets is found to re-open by approximately 10°. before closing again. During both the opening and closing phases, the two leaflets exhibit asymmetric motion, i.e., one leaflet opens/closes faster than the other.

The sinus geometry and curvature of the aortic arch were found to have a significant impact on the leaflet motion. Recall that the current study employed identical valve geometry and incoming flow condition as in Borazjani *et al.*[2] and the only difference between these two studies is the aortic geometry. The asymmetric leaflet motion observed in the current anatomic case was also observed in the straight aorta case. As discussed in Borazjani *et al.*,[2]

in the straight aorta case the asymmetric motion of the two leaflets arises naturally as a result of flow instability since in that case the geometry of the valve as well as the aorta is symmetric. In the current study, however, the geometry of the aorta is asymmetric and highly three-dimensional. Such an asymmetric geometry enhances the effect of natural flow instability in the anatomic case, leading to a more pronounced asymmetric motion than in the straight aorta case. The leaflets were also found to open faster but close slower in the current case than the straight aorta case. Such impact of geometry on leaflet motion clearly underscores the importance of patient-specific studies of BMHV hemodynamics.

The delayed valve closing in the anatomic case deserves special attention and discussion. Such a delayed closing of BMHV is in striking contrast to the motion of natural heart valves, which are typically seen to reach the fully closed state at the onset of the reverse flow.[33] The delayed closure of BMHV is a well known phenomenon [34,39] and could be attributed to the hemodynamic difference between these different types of valves. The closure of the natural/bioprosthetic valves is facilitated by the pressure difference between the two sides of valve leaflets. As seen in the sketch shown in Fig. 15a, the leaflets of natural valves divide the flow lumen into two separate regions: the fast flow region located in the center of flow lumen and the recirculation flow region located between the leaflets and sinus wall. As shown by Lee and Talbot,[25] the pressure field within the fast flow region, when viscous effects are neglected, is primarily driven by the acceleration/deceleration of the incoming flow ($\frac{\partial U}{\partial t} = -\frac{\partial p}{\partial l}$, where l denotes the flow direction). During the late systole, the flow in the central region decelerates, which causes a significant pressure drop in the central lumen region. The flow in the recirculation region, however, does not undergo the same amount of deceleration as in the central flow region. This important difference in local hemodynamics leads to higher pressure at the sinus side of each leaflet and creates a pressure force pointing toward the closing direction of each leaflet. In contrast to natural valves, the leaflets of BMHV are located in the central flow region. The velocities of flows on the two sides of each leaflet are practically the same (Fig. 15b). During the deceleration phase of cardiac systole, the flow fields on the two sides of each leaflet undergo similar amount of flow deceleration. As a result, no closing pressure force is created by the flow deceleration and the closure of the leaflets has to wait until the onset of reverse flow. The delayed closure has a direct unfavorable impact on the valve performance, causing larger regurgitant blood volume in BMHV than in natural/bioprosthetic valves. With the development of advanced numerical simulations tools, such as the one used in the current study, it is now possible to optimize valve design and placement to reduce regurgitation.

Our results clearly show the importance of aorta geometry on the flow physics, shear stress, and pressure drop. The flow in the anatomic aorta is different from the flow in the straight aorta. The flow becomes unstable slower later in the cardiac cycle in the anatomic aorta due to the curvature of the aorta and reattaches faster to the sinus region, which retards and diffuses the jets coming out of the valve. The histogram of local shear showed that in most of the domain the shear values were low but there were regions with high values. The regions of high shear value were found to be near the leaflets and in the aortic arch. The anatomic aorta has larger regions of high shear. The larger regions of high shear are associated with the curvature of the aorta. The maximum value of the shear and the size of regions of high shear as well as the pressure drop correlate with the incoming flow rate.

The results of this work clearly underscore the effect of the curved aorta geometry relative to the straight one. Nevertheless, other parameters that can affect the flow physics and shear stress values are compliance of the aortic walls and the implementation of realistic upstream (left ventricle) and downstream boundary conditions. The blood flow distribution between different arteries that branch from the aorta is also important in determining the downstream boundary conditions as shown in Grinberg and Karniadakis.[18] The relative importance of

these parameters and the extent of their effect on the flow physics, shear stress, and leaflet kinematics is not known and needs further research. In this work we have assumed the blood to be a Newtonian fluid. This assumption is reasonable for larger arteries such as the aorta. However, in cases where the size of the flow domain is in the same order of magnitude as the blood cell size (i.e., small arteries) the non-Newtonian effects should be taken into account. New work along these lines is currently under way in our group and results will be reported in future communications. Resolving the above major challenges and coupling the computational algorithm to imaging modalities can provide a strong computational tool for patient-specific valve design and implantation planning.

Acknowledgments

This work was supported by NIH Grant RO1-HL- 07262 and the Minnesota Supercomputing Institute. We thank Ajit Yoganathan and the members of the Cardiovascular Fluid Mechanics Laboratory for providing us with the anatomic aorta geometry used in this study.

References

1. Borazjani, I. PhD thesis. University of Minnesota; June. 2008 Numerical simulations of fluid/structure interaction problems in biological flows.
2. Borazjani I, Ge L, Sotiropoulos F. Curvilinear immersed boundary method for simulating fluid structure interaction with complex 3d rigid bodies. J Comput Phys. 2008; 227(16):7587–7620. [PubMed: 20981246]
3. Borazjani I, Sotiropoulos F. Numerical investigation of the hydrodynamics of carangiform swimming in the transitional and inertial flow regimes. J Exp Biol. 2008; 211:1541–1558. [PubMed: 18456881]
4. Chandran KB, Cabell GN, Khalighi B, Chen CJ. Laser anemometry measurements of pulsatile flow past aortic valve prostheses. J Biomech. 1983; 16(10):865–873. [PubMed: 6643525]
5. Cheng R, Lai YG, Chandran KB. Two-dimensional fluid–structure interaction simulation of bileaflet mechanical heart valve flow dynamics. J Heart Valve Dis. 2003; 12(6):772–780. [PubMed: 14658820]
6. Cheng R, Lai YG, Chandran KB. Three-dimensional fluid–structure interaction simulation of bileaflet mechanical heart valve flow dynamics. Ann Biomed Eng. 2004; 32(11):1471–1483. [PubMed: 15636108]
7. Dasi LP, Ge L, Simon HA, Sotiropoulos F, Yoganathan AP. Vorticity dynamics of a bileaflet mechanical heart valve in an axisymmetric aorta. Phys Fluids. 2007; 19:067105.
8. de Zélicourt D, Pekkan K, Kitajima H, Frakes D, Yoganathan AP. Single-step stereolithography of complex anatomical models for optical flow measurements. J Biomech Eng. 2005; 127:204. [PubMed: 15868804]
9. Ellis JT, Healy TM, Fontaine AA, Saxena R, Yoganathan AP. Velocity measurements and flow patterns within the hinge region of a medtronic parallel bileaflet mechanical valve with clear housing. J Heart Valve Dis. 1996; 5(6):591–599. [PubMed: 8953436]
10. Feng Z, Umezu M, Fujimoto T, Tsukahara T, Nurishi M, Kawaguchi D. In vitro hydrodynamic characteristics among three bileaflet valves in the mitral position. Artif Organs. 2000; 24(5):346–354. [PubMed: 10848675]
11. Ge L, Dasi LP, Sotiropoulos F, Yoganathan AP. Characterization of hemodynamic forces induced by mechanical heart valves: Reynolds vs. viscous stresses. Ann Biomed Eng. 2008; 36(2):276–297. [PubMed: 18049902]
12. Ge L, Leo HL, Sotiropoulos F, Yoganathan AP. Flow in a mechanical bileaflet heart valve at laminar and near-peak systole flow rates: Cfd simulations and experiments. J Biomech Eng. 2005; 127:782. [PubMed: 16248308]
13. Ge L, Sotiropoulos F. A numerical method for solving the 3d unsteady incompressible navierstokes equations in curvilinear domains with complex immersed boundaries. J Comput Phys. 2007; 225(2):1782–1809. [PubMed: 19194533]

14. Gilmanov A, Sotiropoulos F. A hybrid cartesian/immersed boundary method for simulating flows with 3d, geometrically complex, moving bodies. J Comput Phys. 2005; 207(2):457.
15. Grigioni M, Daniele C, D'Avenio G, Barbaro V. The influence of the leaflets curvature on the flow field in two bileaflet prosthetic heart valves. J Biomech. 2001; 34(5):613–621. [PubMed: 11311702]
16. Grigioni M, Daniele C, D'Avenio G, Barbaro V. Evaluation of the surface-averaged load exerted on a blood element by the Reynolds shear stress field provided by artificial cardiovascular devices. J Biomech. 2002; 35(12):1613–1622. [PubMed: 12445614]
17. Grigioni M, Daniele C, Del Gaudio C, Morbiducci U, Balducci A, D'Avenio G, Barbaro V. Three-dimensional numeric simulation of flow through an aortic bileaflet valve in a realistic model of aortic root. ASAIO J. 2005; 51(3):176. [PubMed: 15968945]
18. Grinberg L, Karniadakis GE. Outflow boundary conditions for arterial networks with multiple outlets. Ann Biomed Eng. 2008; 36(9):1496–1514. [PubMed: 18612828]
19. Heart Disease and Stroke Statistics. 2007 Update. Technical report. American Heart Association; 2007.
20. Huang ZJ, Merkle CL, Abdallah S, Tarbell JM. Numerical simulation of unsteady laminar flow through a tilting disk heart valve: prediction of vortex shedding. J Biomech. 1994; 27(4):391–402. [PubMed: 8188720]
21. Hunt, JCR.; Wray, AA.; Moin, P. Eddies, streams, and convergence zones in turbulent flows. Studying Turbulence Using Numerical Simulation Databases, 2. Proceedings of the 1988 Summer Program (SEE N89- 2453818-34); 1988. p. 193-208.
22. Irons BM, Tuck RC. A version of the aitken accelerator for computer iteration. Int J Numer Methods Eng. 1969; 1(3):275–277.
23. King MJ, Corden J, David T, Fisher J. A three-dimensional, time-dependent analysis of flow through a bileaflet mechanical heart valve: comparison of experimental and numerical results. J Biomech. 1996; 29(5):609–618. [PubMed: 8707787]
24. Kleine P, Perthel M, Nygaard H, Hansen SB, Paulsen PK, Riis C, Laas J. Medtronic hall versus st. jude medical mechanical aortic valve: downstream turbulences with respect to rotation in pigs. J Heart Valve Dis. 1998; 7(5):548–555. [PubMed: 9793855]
25. Lee CSF, Talbot L. A fluid-mechanical study of the closure of heart valves. J Fluid Mech. 1979; 91(1):41–63.
26. Liu JS, Lu PC, Chu SH. Turbulence characteristics downstream of bileaflet aortic valve prostheses. J Biomech Eng. 2000; 122(2):118–124. [PubMed: 10834151]
27. Manning KB, Kini V, Fontaine AA, Deutsch S, Tarbell JM. Regurgitant flow field characteristics of the st. jude bileaflet mechanical heart valve under physiologic pulsatile flow using particle image velocimetry. Artif Organs. 2003; 27(9):840–846. [PubMed: 12940907]
28. Marshall I, Zhao S, Papathanasopoulou P, Hoskins P, Xu XY. MRI and CFD studies of pulsatile flow in healthy and stenosed carotid bifurcation models. J Biomech. 2004; 37(5):679–687. [PubMed: 15046997]
29. Mok, DP.; Wall, WA.; Ramm, E. Accelerated iterative substructuring schemes for instationary fluid–structure interaction. First MIT Conference on Computational Fluid and Solid Mechanics; 2001. p. 1325-1328.
30. Nyboe C, Funder JA, Smerup MH, Nygaard H, Hasenkam JM. Turbulent stress measurements downstream of three bileaflet heart valve designs in pigs. Eur J Cardiothorac Surg. 2006; 29(6): 1008–1013. [PubMed: 16675253]
31. Nygaard H, Paulsen PK, Hasenkam JM, Pedersen EM, Rovsing PE. Turbulent stresses downstream of three mechanical aortic valve prostheses in human beings. J Thorac Cardiovasc Surg. 1994; 107(2):438–446. [PubMed: 8302062]
32. Pekkan K, Zlicourt D, Ge L, Sotiropoulos F, Frakes D, Fogel MA, Yoganathan AP. Physics-driven cfd modeling of complex anatomical cardiovascular flowsa tcpc case study. Ann Biomed Eng. 2005; 33(3):284–300. [PubMed: 15868719]
33. Peskin CS. The fluid dynamics of heart valves: experimental, theoretical, and computational methods. Annu Rev Fluid Mech. 1982; 14(1):235–259.

34. Scotten LN, Walker DK. New laboratory technique measures projected dynamic area of prosthetic heart valves. J Heart Valve Dis. 2004; 13(1):120–32. [PubMed: 14765850]

35. Sotiropoulos F, Borazjani I. A review of state-of-the-art numerical methods for simulating flow through mechanical heart valves. Med Biol Eng Comput. 2009; 47:245–256. [PubMed: 19194734]

36. Steinman DA, Milner JS, Norley CJ, Lownie SP, Holdsworth DW. Image-based computational simulation of flow dynamics in a giant intracranial aneurysm. Am J Neuroradiol. 2003; 24(4):559–566. [PubMed: 12695182]

37. Travis BR, Leo HL, Shah PA, Frakes DH, Yoganathan AP. An analysis of turbulent shear stresses in leakage flow through a bileaflet mechanical prostheses. J Biomech Eng. 2002; 124(2):155–165. [PubMed: 12002124]

38. Vorp DA, Steinman DA, Ethier CR. Computational modeling of arterial biomechanics. Comput Sci Eng. 2001; 3(5):51–64.

39. Yoganathan AP, He Z, Jones SC. Fluid mechanics of heart valves. Annu Rev Biomed Eng. 2004; 6:331–362. [PubMed: 15255773]

40. Yoganathan AP, Woo YR, Sung HW. Turbulent shear stress measurements in the vicinity of aortic heart valve prostheses. J Biomech. 1986; 19(6):433–442. [PubMed: 2943742]

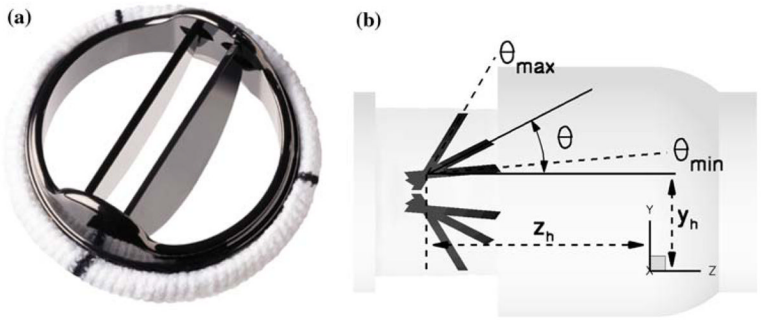

FIGURE 1.

(a) A typical bi-leaflet mechanical heat valve (St. Jude Regent). (b) The definition of leaflet angle θ. The leaflets hinge axis is placed parallel to x-axis of the global frame of reference at position (y_h, z_h) in the YZ plane.

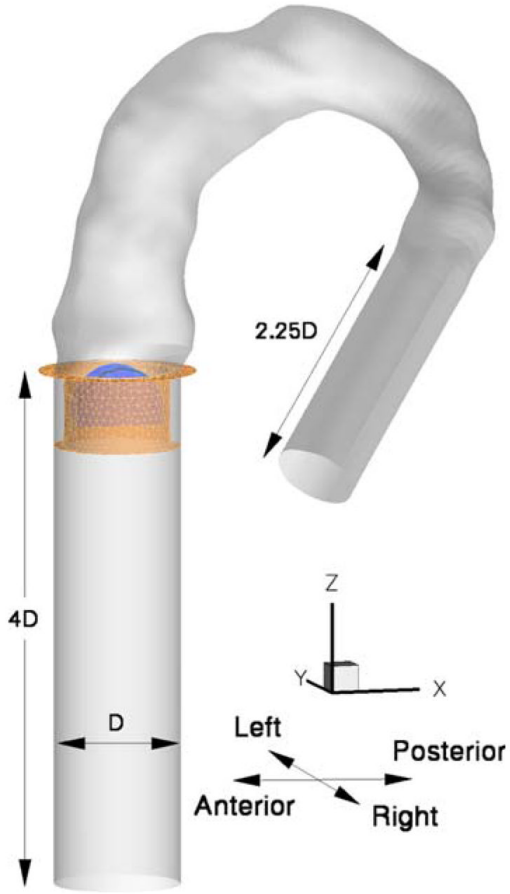

FIGURE 2.
The anatomically realistic aorta geometry reconstructed from MRI data and the straight inlet and outlet additions.

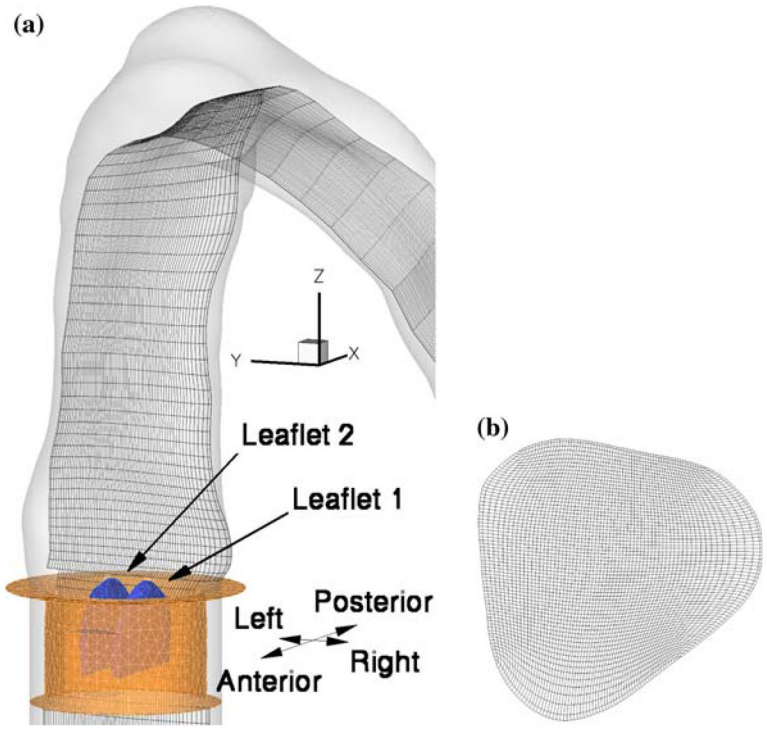

FIGURE 3.
The computational grid for the BMHV anatomic aorta simulations. (a) Side view showing the background curvilinear grid used to discretize the empty anatomic aorta and the unstructured mesh used to discretize the leaflets and the housing. (b) Cross-sectional view of the background grid in the sinus area. For clarity, only every third grid is plotted.

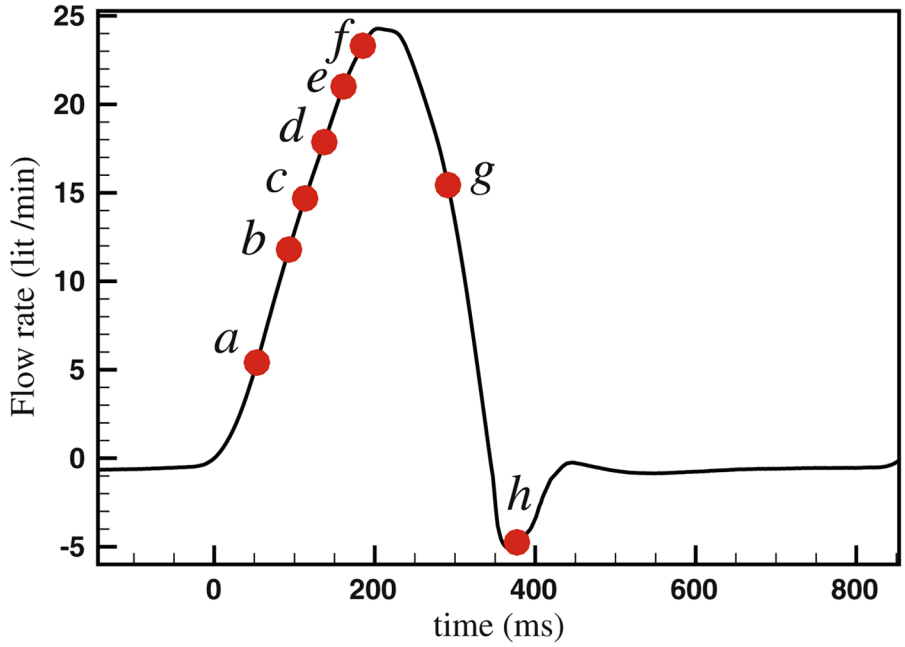

FIGURE 4.
Physiological incoming flow waveform specified at the inlet. The time instants in the cardiac cycle in which the flow is visualized are marked with red circles *a*, *b*, *c*,….

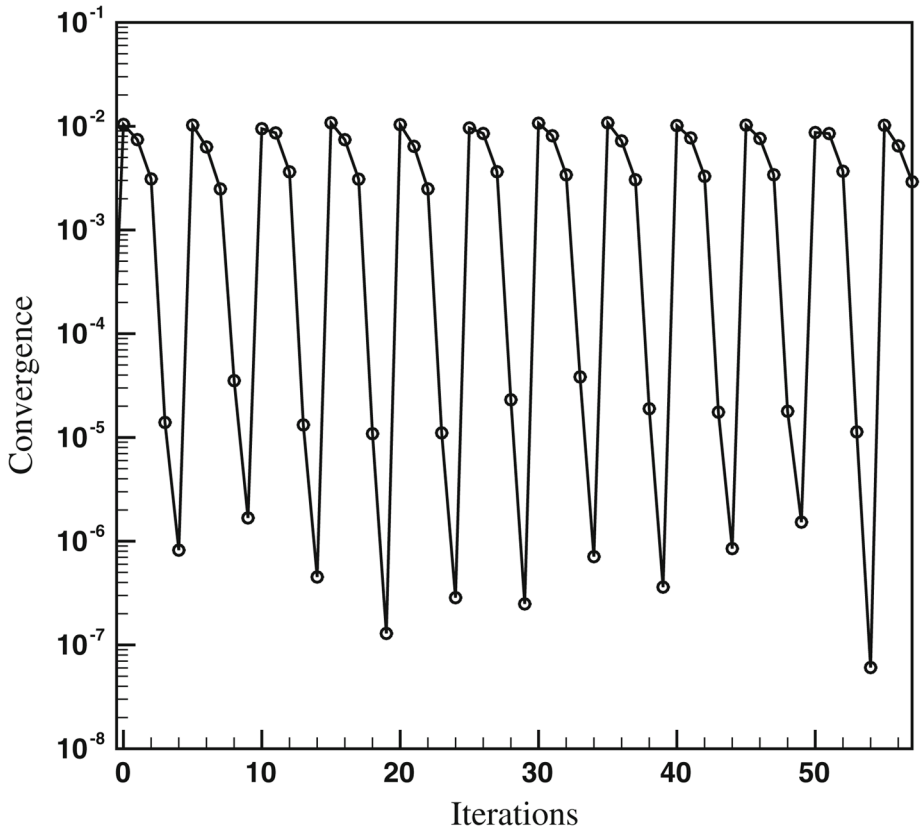

FIGURE 5.
FSI convergence of strong-coupling with under-relaxation and the Aitken acceleration technique for 12 physical time steps (each peak represents one physical time step). Typically 4–5 sub-iterations were enough for the FSI to converge for each physical time step.

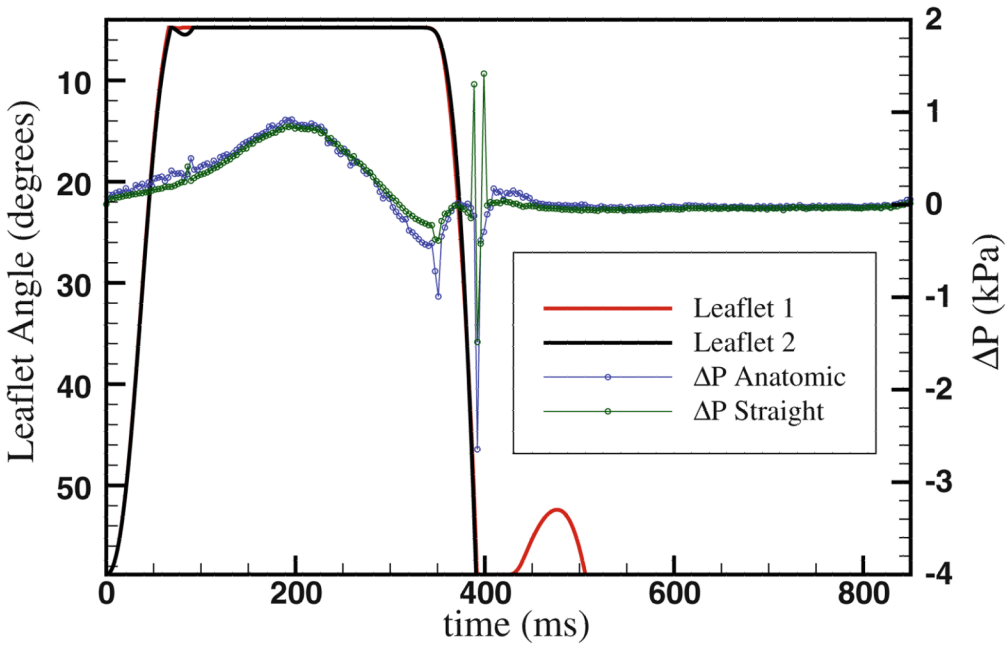

FIGURE 6.
Leaflet kinematics for the BMHV in an anatomic aorta and pressure drop through the BMHV for anatomic and straight aortas.

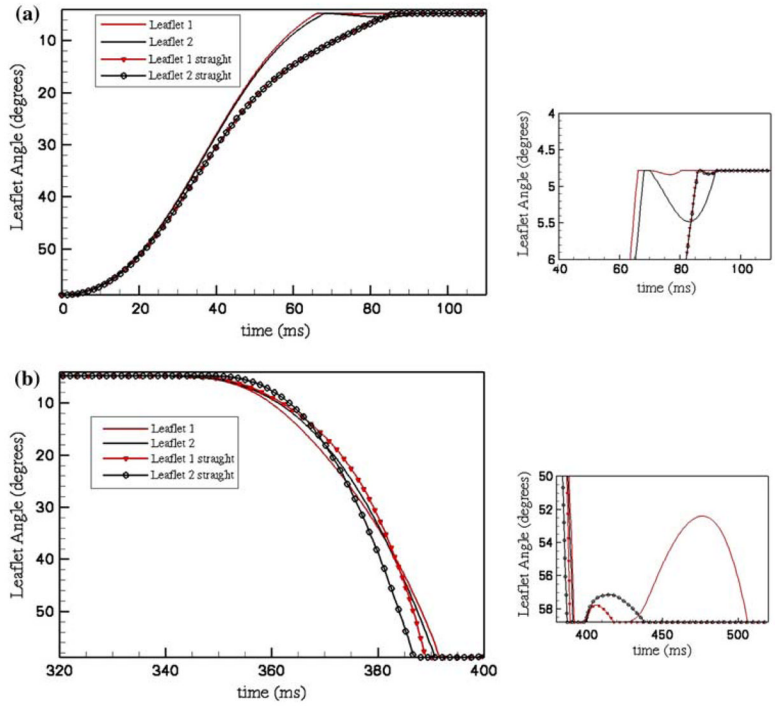

FIGURE 7.

Comparison of leaflet kinematics for the BMHV in an anatomic and a straight aorta during (a) opening and (b) closing. The insets on the right are zoomed in to show the rebound effect.

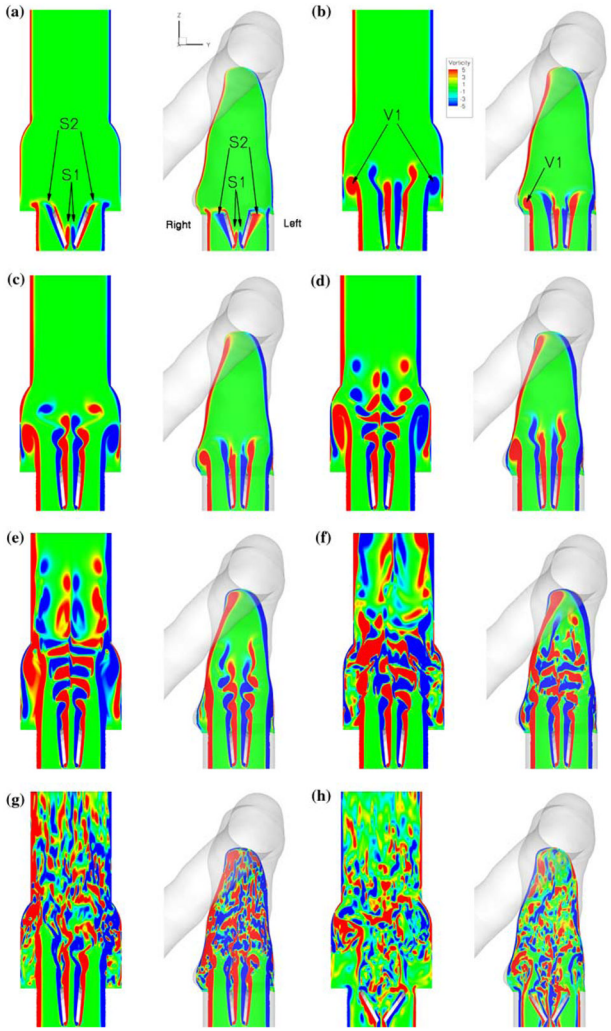

FIGURE 8.

Comparison of instantaneous out-of-plane non-dimensional vorticity ($\Omega D/U$) contours for an anatomic aorta vs. a straight aorta on the midplane of the valve. *a*, *b*, *c*,… correspond to the time instant marked in Fig. 4 within the cardiac cycle.

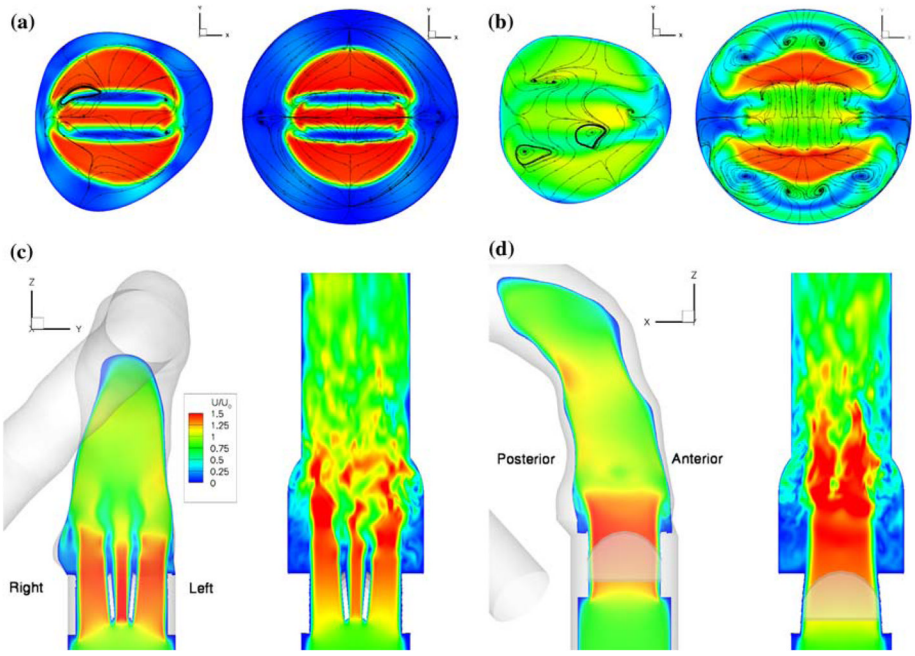

FIGURE 9.

Comparison of instantaneous contours velocity magnitude U non-dimensionalized by the inlet maximum velocity magnitude U_0 = 0.8 m/s for an anatomic aorta vs. a straight aorta at time instant *d* marked in Fig. 4 on different cross-sections and plane: (a) cross-section just at the end of leaflets; (b) cross-section 0.5D downstream of the leaflets; (c) valve midplane (x = 0); (d) valve top side jet plane (y = 0.25D).

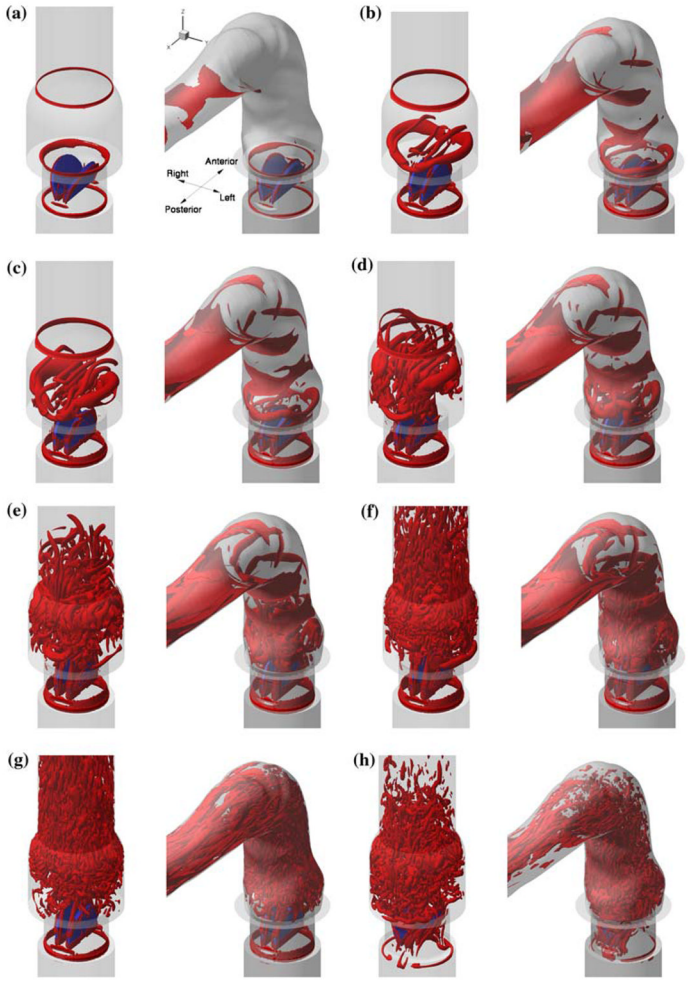

FIGURE 10.

Comparison of instantaneous vortical structures visualized by iso-surfaces of q-criteria for an anatomic aorta vs. a straight aorta. *a*, *b*, *c*,… correspond to the time instant marked in Fig. 4 within the cardiac cycle.

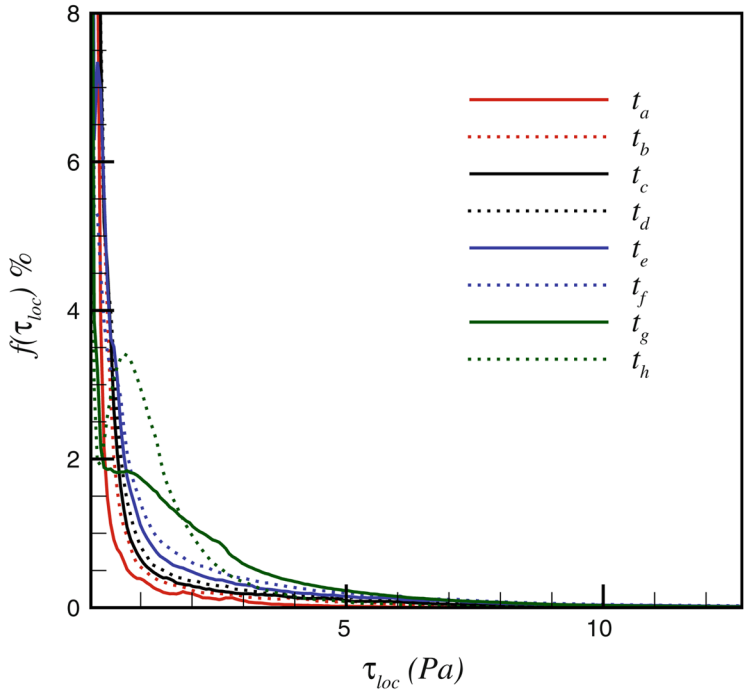

FIGURE 11.

Histograms of local maximum shear τ_{loc} in the anatomic aorta. *f* is the percentile of the number of occurrences of a shear value τ_{loc} values in intervals with the width $\Delta \tau_{loc} = 0.064$ Pa to the total number of occurrences. *a*, *b*, *c*,… correspond to the time instant marked in Fig. 4 within the cardiac cycle.

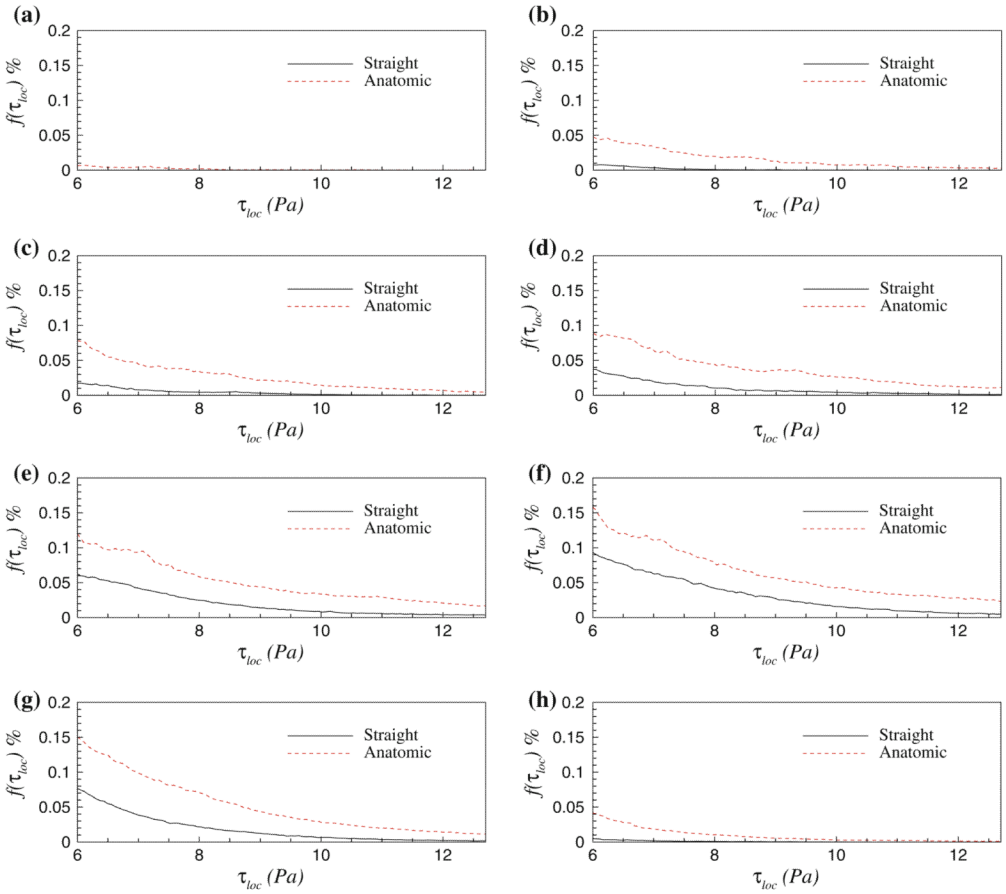

FIGURE 12.

Histograms of local maximum shear τ_{loc} in the straight and anatomic aortas. *f* is the percentile of the number of occurrences of a shear value τ_{loc} values in intervals with the width $\Delta\ \tau_{loc} = 0.064$ Pa to the total number of occurrences. *a*, *b*, *c*,… correspond to the time instant marked in Fig. 4 within the cardiac cycle.

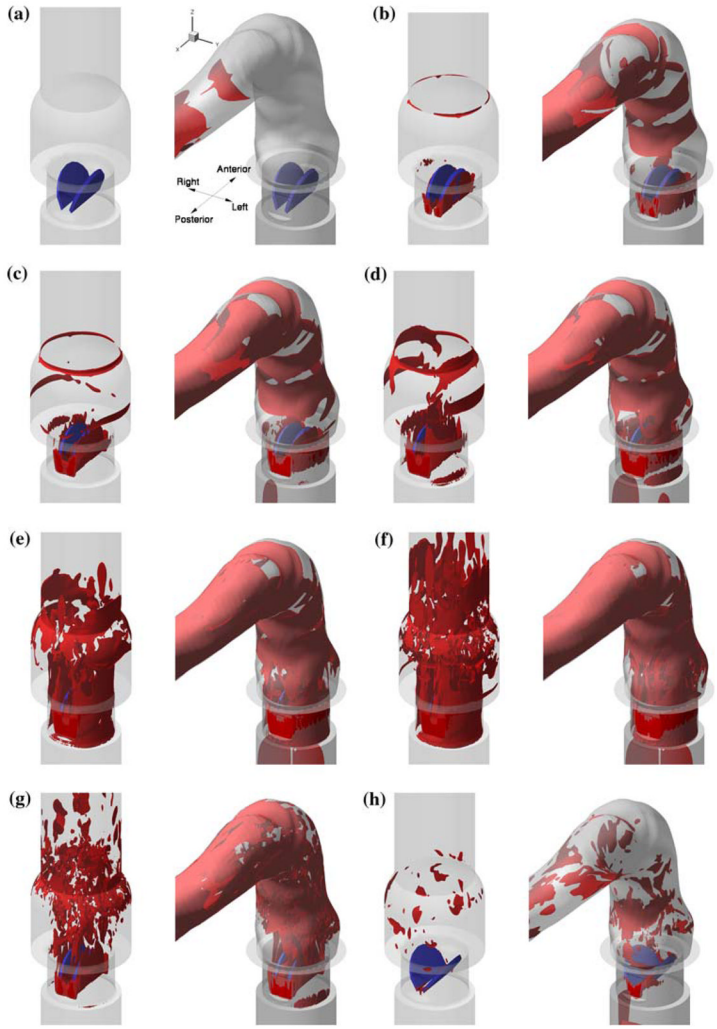

FIGURE 13.

Comparison of instantaneous iso-surfaces of local maximum shear τ_{loc} = 6.4 Pa for an anatomic aorta vs. a straight aorta. *a*, *b*, *c*,… correspond to the time instant marked in Fig. 4 within the cardiac cycle.

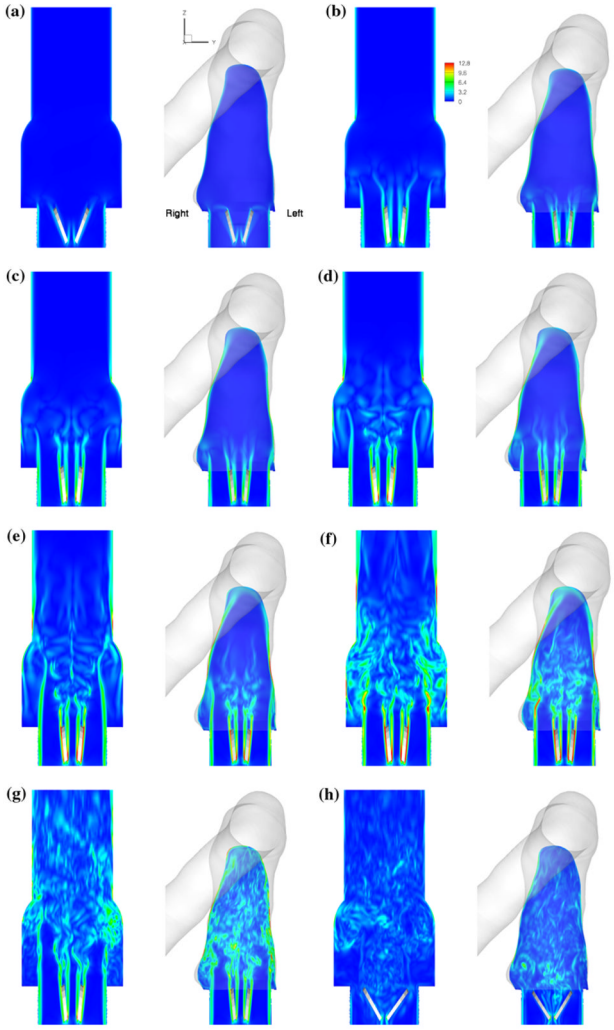

FIGURE 14.
Comparison of instantaneous local maximum shear τ_{loc} contours over the midplane of the valve for an anatomic aorta vs. a straight aorta. *a*, *b*, *c*,… correspond to the time instant marked in Fig. 4 within the cardiac cycle. Unit: Pa.

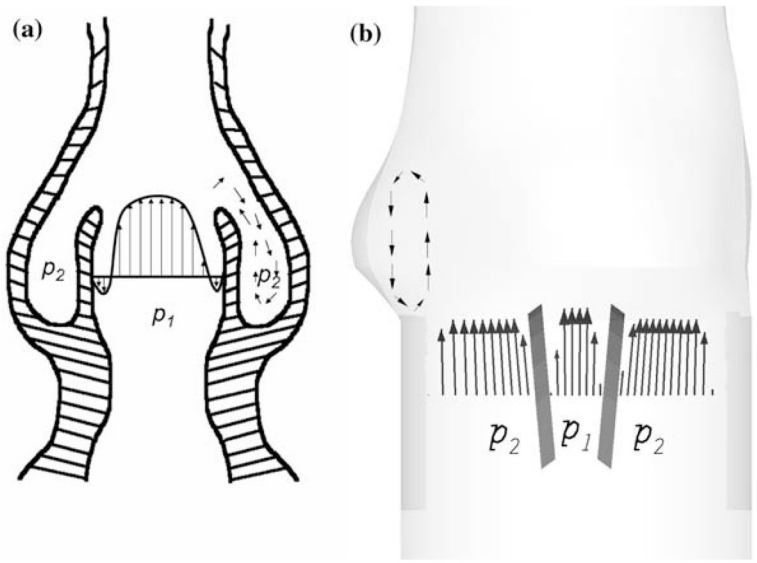

FIGURE 15.
Sketch showing the velocity profile on the midplane of valve and the pressure on each side of (a) natural valves and (b) mechanical valves.